The oceanic anthropogenic CO_2 sink: Storage, air-sea fluxes, and transports over the industrial era

Tim DeVries[1]

[1] Department of Atmospheric and Oceanic Sciences, University of California, Los Angeles, California, USA

Abstract This study presents a new estimate of the oceanic anthropogenic CO_2 (C_{ant}) sink over the industrial era (1780 to present), from assimilation of potential temperature, salinity, radiocarbon, and CFC-11 observations in a global steady state ocean circulation inverse model (OCIM). This study differs from previous data-based estimates of the oceanic C_{ant} sink in that dynamical constraints on ocean circulation are accounted for, and the ocean circulation is explicitly modeled, allowing the calculation of oceanic C_{ant} storage, air-sea fluxes, and transports in a consistent manner. The resulting uncertainty of the OCIM-estimated C_{ant} uptake, transport, and storage is significantly smaller than the comparable uncertainty from purely data-based or model-based estimates. The OCIM-estimated oceanic C_{ant} storage is 160–166 PgC in 2012, and the oceanic C_{ant} uptake rate averaged over the period 2000–2010 is 2.6 PgC yr^{-1} or about 30% of current anthropogenic CO_2 emissions. This result implies a residual (primarily terrestrial) C_{ant} sink of about 1.6 PgC yr^{-1} for the same period. The Southern Ocean is the primary conduit for C_{ant} entering the ocean, taking up about 1.1 PgC yr^{-1} in 2012, which represents about 40% of the contemporary oceanic C_{ant} uptake. It is suggested that the most significant source of remaining uncertainty in the oceanic C_{ant} sink is due to potential variability in the ocean circulation over the industrial era.

1. Introduction

Human activities such as fossil fuel burning, cement production, and deforestation have driven large amounts of CO_2 into the atmosphere over the industrial era (~1780 to present), with associated changes in the Earth's climate [*Hegerl et al.*, 2007]. The ocean represents a significant sink of anthropogenic CO_2 emissions, having absorbed roughly 20–40% of CO_2 emitted due to human activities over the industrial era [*Ciais et al.*, 2013]. Despite its importance in the global carbon cycle and in mitigating anthropogenic climate change, significant uncertainties remain in quantifying the global oceanic anthropogenic CO_2 sink [*Wang et al.*, 2012; *Khatiwala et al.*, 2013]. These uncertainties stem from uncertainties and biases in data-based methodologies for inferring oceanic anthropogenic CO_2 storage and in dynamical ocean models used to infer the air-sea fluxes and oceanic transport of anthropogenic CO_2 (C_{ant}).

Although some recent studies have been able to infer oceanic anthropogenic CO_2 uptake by repeated direct measurements of the in situ dissolved inorganic carbon (DIC) concentration [e.g., *Wanninkhof et al.*, 2010; *Bates et al.*, 2012], such measurements are too sparse to allow a global estimate of the oceanic C_{ant} sink and do not extend far back enough in time to allow historical estimates of the oceanic C_{ant} sink. Given this lack of direct observation of the oceanic C_{ant} concentration, several indirect methods have been devised for estimating anthropogenic CO_2 storage at a global scale and over long time periods. The first global estimate of oceanic C_{ant} storage used the ΔC^* method [*Gruber et al.*, 1996; *Sabine et al.*, 2004]. This and other "back-calculation" methods (see review by *Sabine and Tanhua* [2010]) estimate C_{ant} concentrations by removing the preindustrial or "natural" dissolved inorganic carbon (DIC) component using a combination of water mass and age tracers. Unfortunately, these back-calculation schemes suffer from significant errors and biases including assumptions of constant stoichiometric ratios, neglect of mixing when calculating water mass ages, and assumptions of constant air-sea disequilibrium [*Gruber et al.*, 1996; *Matsumoto and Gruber*, 2005]. More recently, other methods have been employed that do not depend on back calculation, but instead rely on indirectly inferring oceanic C_{ant} uptake from transient tracer observations. *Waugh et al.* [2006] used chlorofluorocarbon (CFC) observations to constrain the ocean's transit time distribution (TTD), from which the oceanic uptake and storage of C_{ant} was inferred. The uncertainties associated with the TTD method are large due to limitations of the data used to constrain the TTD, the parameterized form of the

TTD, and assumptions made about the air-sea disequilibrium [*Waugh et al.*, 2006]. More recently, *Khatiwala et al.* [2009] estimated the ocean's TTD using a more general Green Function (GF) approach, allowing them to derive a four-dimensional estimate of the oceanic anthropogenic CO_2 sink over the industrial era. The GF estimate was substantially improved over previous estimates by the use of multiple tracers to constrain the TTD and by a more realistic treatment of air-sea gas exchange, but uncertainties associated with the GF method are still large, due to the underconstrained nature of the GF inversion that must be regularized using a maximum entropy approach [*Khatiwala et al.*, 2009; *Holzer et al.*, 2010]. To reduce these uncertainties, *Khatiwala et al.* [2013] used results from a dynamical ocean model to help constrain some of the GF parameters; this practice, however, may introduce other model-dependent errors.

A significant disadvantage of all of the above methods is that they do not provide information about the air-sea fluxes or internal oceanic transport of anthropogenic CO_2 over time (although the GF approach does give aggregated air-sea fluxes over large regions over time [*Khatiwala et al.*, 2013]). The air-sea exchange and interior transport of anthropogenic carbon in the ocean have typically been estimated by assimilating data-based estimates of C_{ant} storage into dynamical ocean general circulation models (OGCMs) [e.g., *Mikaloff-Fletcher et al.*, 2006; *Gerber and Joos*, 2010; *Gerber et al.*, 2009; *Gruber et al.*, 2009]. This means that the inferred transports and air-sea fluxes inherit both errors from the method used to determine oceanic C_{ant} concentrations and errors from the underlying OGCM. One study suggests that the two sources of error are approximately equal in magnitude, causing up to 100% uncertainties in regional air-sea fluxes and transports of anthropogenic CO_2 [*Gerber et al.*, 2009].

Given the uncertainties associated with both data-based and the model-based approaches to quantifying the oceanic C_{ant} sink, a promising approach is to assimilate the observations used to indirectly estimate oceanic C_{ant} concentrations directly into an ocean circulation model in order to constrain air-sea gas exchange and ocean ventilation rates, and then use the resulting optimized model to estimate the oceanic uptake, storage, and transport of C_{ant}. Such an approach has been used previously to estimate ocean ventilation rates and anthropogenic CO_2 uptake. Some of the earliest estimates of oceanic anthropogenic CO_2 uptake relied on box diffusion models that were constrained by radiocarbon ($\Delta^{14}C$) observations [e.g., *Oeschger et al.*, 1975]. More recently, the Estimating the Circulation and Climate of the Ocean (ECCO) consortium assimilated global temperature and salinity data into a three-dimensional OGCM, which was then used to simulate the uptake and transport of anthropogenic CO_2 by the ocean [*Graven et al.*, 2012; *Khatiwala et al.*, 2013]. A major shortcoming of the ECCO model is that ventilation tracers such as $\Delta^{14}C$ and chlorofluorocarbons (CFCs) were not assimilated. It has been shown that even models that reproduce temperature and salinity distributions well may still have deficiencies in ventilation that can best be identified by simulating $\Delta^{14}C$ and CFCs [*England and Maier-Reimer*, 2001]. *Gerber and Joos* [2013] assimilated $\Delta^{14}C$ and CFC-11 observations into a global coarse resolution ocean model using an ensemble Kalman filter approach, which improved the representation of ocean ventilation and yielded more realistic oceanic anthropogenic CO_2 uptake than in a model that only assimilated temperature and salinity observations. However, the coarse resolution of that model, as well as the limited number of tunable parameters, resulted in large model-data discrepancies and therefore potentially large model errors.

Here I report results from a new estimate of the oceanic anthropogenic CO_2 sink that addresses many of the issues raised above. In this study, an adjoint approach is used to bring a global ocean circulation inverse model (OCIM) into consistency with global observations of potential temperature, salinity, radiocarbon ($\Delta^{14}C$), and CFC-11. These tracers are assimilated into the OCIM to obtain optimal estimates of the climatological mean (steady state) ocean circulation, ventilation, and air-sea gas exchange rates. The optimized circulation and air-sea gas exchange rates from this model are then used to simulate the oceanic uptake of C_{ant} over the industrial era.

The main advantages of this study compared to previous work are threefold. First, in addition to assimilating temperature and salinity, both $\Delta^{14}C$ and CFC-11 are assimilated, which provide strong constraints on ocean ventilation rates and on C_{ant} uptake [e.g., *England and Maier-Reimer*, 2001; *Waugh et al.*, 2006; *Graven et al.*, 2012]. Second, the entire three-dimensional ocean circulation field is adjusted during the inversion process to achieve optimal consistency with the observed tracer distributions. This results in a far better match between modeled and observed tracer fields than achieved by previous models that assimilated $\Delta^{14}C$ and CFC-11 [e.g., *Gerber and Joos*, 2013]. Third, unlike previous studies that have assimilated data-based C_{ant} estimates into OGCMs to estimate air-sea fluxes and transport of anthropogenic CO_2 [e.g., *Mikaloff-Fletcher et al.*,

2006; *Gerber and Joos*, 2010; *Gerber et al.*, 2009; *Gruber et al.*, 2009], this study produces three-dimensional estimates of oceanic C_{ant} uptake, storage, and transport that are internally consistent with the data used to estimate both the C_{ant} concentration and the underlying ocean circulation. This internal consistency is shown to reduce the uncertainty of oceanic C_{ant} uptake, storage, and transport compared to previous studies. A significant caveat, however, is that any changes in the ocean C_{ant} sink due to ocean circulation variability are not captured by this approach, since a steady state ocean circulation is assumed.

The underlying model and data assimilation approach used here is most similar to that of *Schlitzer* [2007], who also assimilated radiocarbon and CFC observations into a global ocean model to constrain deep ocean ventilation rates. Among other differences, the model used in this study is of higher spatial resolution than that of *Schlitzer* [2007] and includes improved parameterizations of subgridscale processes. A detailed description of the ocean circulation inverse model used here is given in section 2. The OCIM is applied to estimate the oceanic C_{ant} sink over the industrial era in section 3. Section 4 discusses implications of these findings for the terrestrial carbon sink, and section 5 summarizes the results and discusses remaining uncertainties in the oceanic C_{ant} sink.

2. Methods

2.1. Ocean Circulation Inverse Model

The ocean circulation model used in this study was introduced by *DeVries and Primeau* [2011] and has been used extensively to study various aspects of the ocean's circulation and biogeochemistry [*DeVries et al.*, 2012a, 2012b, 2013; *Primeau et al.*, 2013; *Waugh et al.*, 2013; *Holzer and Primeau*, 2013; *Weber and Deutsch*, 2012]. The basic theory and methodology behind the model is described by *DeVries and Primeau* [2011]. This section provides a brief description of the model and of how it is extended to estimate the oceanic C_{ant} sink.

The underlying dynamical ocean model is based on a steady state linear momentum balance together with the continuity equation, which when discretized on the model grid can be cast in terms of a matrix equation

$$\mathbf{Mx} + \mathbf{f} = \mathbf{e}, \tag{1}$$

where $\mathbf{x} = [u\ v\ w\ h]$ is the dynamical model state including the horizontal and vertical velocity components and the sea surface height, and $\mathbf{M}$ is a matrix operator that enforces mass continuity and balance among the frictional, Coriolis, and barotropic pressure forces, and the forces in $\mathbf{f}$ which include the imposed surface wind stress and baroclinic pressure forces. Previous versions of the OCIM parameterized frictional forces with Laplacian viscosity terms, but here we use a simple linear (Rayleigh) drag $\lambda = 10^{-6}\ \text{s}^{-1}$, which gives nearly identical results. Equation (1) is discretized on an Arakawa B-grid with 2° horizontal resolution and 24 unevenly spaced vertical levels, ranging in thickness from 30 m at the surface to 500 m at depth. The OCIM differs fundamentally from standard free-running OGCMs in that the baroclinic pressure forces are not computed from internally simulated temperature and salinity but are diagnosed from climatological observed density fields. With this linear formulation, equation (1) can be solved in under 1 s, after a suitable factorization of the matrix $\mathbf{M}$.

A "model error" term $\mathbf{e}$ in equation (1) takes into account errors in the model state $\mathbf{x}$ that might result from errors in the climatological density and wind stress fields (i.e., errors in $\mathbf{f}$), as well as errors resulting from the discretization of the governing equations, the steady state assumption, and neglect of nonlinear terms in the momentum balance. The components of $\mathbf{e}$ corresponding to the mass-continuity equation are taken to be identically zero, while the other components of $\mathbf{e}$ are initially assumed to be zero and are iteratively adjusted during the inversion process to achieve consistency with observed tracer fields (see section 2.2). Examining the spatial distribution of the error terms for the u momentum and v momentum equations reveals that the error terms are largest near boundaries and in particular those regions that experience large eddy variability and fast ocean currents, for example, in the vicinity of western boundary currents and Antarctic Circumpolar Current (ACC) regions (Figure 1). This spatial distribution of the error terms is consistent with prior expectations. The boundary regions are areas of steep topography which are poorly resolved by the coarse 2° model grid, while the western boundary current and ACC regions experience high degrees of eddy variability and have fast-moving ocean currents. Thus, these are all regions in which a steady state frictional-geostrophic balance may break down, necessitating adjustments to the initial momentum balance.
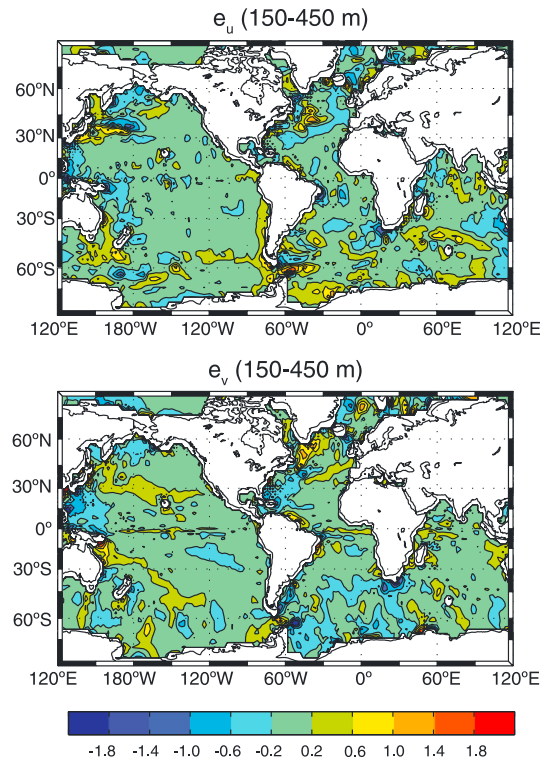
Figure 1. Model error terms averaged over the depth interval 150–450 m for (a) the zonal momentum balance (e_u) and (b) the meridional momentum balance (e_v). Units are 10^{-6} m s^{-2}.

The modeled velocity fields from the solution to equation (1), along with parameterized diffusive terms, are used to form a matrix transport operator $\mathcal{T}$, which is used to simulate tracers according to the tracer conservation equation

$$d\mathbf{c}/dt + \mathcal{T}\mathbf{c} = \mathbf{s}, \qquad (2)$$

where $\mathbf{c}$ is a generic tracer and $\mathbf{s}$ is a tracer source-sink term. While the advective (velocity) terms in $\mathcal{T}$ are optimized, the diffusive terms are not. Previous versions of the model used constant Laplacian horizontal and vertical diffusion, but the version used here orients diffusion along isopycnals [*Redi*, 1982]. The isopycnal diffusivity is parameterized according to *Griffies et al.* [1998] using a uniform isopycnal diffusivity K_I. A uniform background vertical diffusivity K_V is also imposed, and vertical diffusivities in the surface mixed layer are parameterized according to the nonlocal K-Profile Parameterization scheme [*Large et al.*, 1994]. The depth of the surface mixed layer is diagnosed from observations of winter mixed layer depths [*de Boyer Montégut et al.*, 2004]. The sensitivity of the model to the values of K_I and K_V is examined as discussed in section 2.3.

The tracers assimilated in this study include potential temperature (Θ), salinity (S), natural or "background" Δ^{14}C, and CFC-11. Natural Δ^{14}C is a steady state approximation of the preindustrial Δ^{14}C distribution [*Key et al.*, 2004]. For all tracers, the source-sink term can be cast in terms of an air-sea flux operating in the top model layer only

$$\mathbf{s} = \frac{k}{\Delta z_1}(\alpha \mathbf{c}_{\text{atm}} - \mathbf{c}) \qquad (3)$$

where $\mathbf{c}_{\text{atm}}$ is the atmospheric tracer concentration, α is a solubility, k is a piston velocity, and Δz_1 is the depth of the first model layer. The source-sink term for Δ^{14}C also includes first-order decay with a rate of $(8266 \text{ years})^{-1}$.

Potential temperature, salinity, and Δ^{14}C are solved at equilibrium ($d\mathbf{c}/dt = 0$), and so transient atmospheric histories of these tracers are not required. For these tracers $\alpha = 1$ and $k = \Delta z_1(30 \text{ days})^{-1}$, and the corresponding "atmospheric" values are included as control parameters of the inverse model (see *DeVries and Primeau* [2011] and section 2.2). The atmospheric history of CFC-11 [*Bullister*, 2011] is used to force a transient simulation of CFC-11 in the model, beginning in 1938 and ending in 2010, with a time step of 1 year. For CFC-11, the piston velocity k is parameterized as a quadratic function of wind speed [e.g., *Wanninkhof*, 1992; *Sweeney et al.*, 2006]

$$k = \gamma \langle u_{10}\rangle^2 (Sc/660)^{-1/2}(1 - f_{\text{ice}}) \qquad (4)$$

where u_{10} is the root-mean-square wind speed at 10 m above the sea surface, Sc is the temperature-dependent Schmidt number, and f_{ice} is the climatological fractional ice cover. The wind speed and ice cover climatologies are the same as those used in Phase 2 of the Ocean Carbon Cycle Model Intercomparison Project (OCMIP-2) [*Najjar and Orr*, 1998]. The coefficient γ controls the wind speed dependence of the piston velocity and is determined as part of the solution to the inverse model.

In addition to the four tracers simulated by the model, air-sea heat (Q_H) and freshwater (Q_F) fluxes are diagnosed from the model solution. This provides two additional constraints on the inverse model [see *DeVries and Primeau*, 2011]. The model state $\mathbf{y}$ of the combined dynamical model and tracer transport model thus includes 10 state variables: $\mathbf{y} = [u\ v\ w\ h\ \Theta\ S\ \Delta^{14}\text{C CFC-11}(t)\ Q_H\ Q_F]$.

2.2. Inversion Procedure

As described in detail by *DeVries and Primeau* [2011], the purpose of the inversion is to minimize an objective function of the form

$$\mathbf{J}(\mathbf{p}) = (\mathbf{y}(\mathbf{p}) - \mathbf{y}^{\text{obs}})^{\mathbf{T}}\Gamma_{yy}^{-1}(\mathbf{y}(\mathbf{p}) - \mathbf{y}^{\text{obs}}) + \frac{1}{\omega^2}(\mathbf{p} - \mathbf{p}_0)^{\mathbf{T}}\Gamma_{pp}^{-1}(\mathbf{p} - \mathbf{p}_0), \tag{5}$$

where $\mathbf{y}(\mathbf{p})$ is the model state vector and $\mathbf{y}^{\text{obs}}$ is a corresponding vector of observations; $\mathbf{p}$ is the set of adjustable "control" parameters of the model, and $\mathbf{p}_0$ is the corresponding prior expected value of the parameters; Γ_{yy} is the covariance matrix for the observations, and Γ_{pp} is the covariance matrix for the control parameters; and ω is a hyperparameter that controls the relative strengths of the data constraints and the parameter constraints. Using a quasi-Newton algorithm along with the adjoint method [see *DeVries and Primeau*, 2011], the minimum of equation (5) typically is found in about 4000 iterations.

The formulation of the covariance matrices has been described in *DeVries and Primeau* [2011]. Here are added additional terms to Γ_{yy} for CFC-11 observations, which have been taken from the Global Ocean Data Analysis Project (GLODAP) [*Key et al.*, 2004] and Carbon In The Atlantic Ocean (CARINA) [*Carbon In The Atlantic Ocean Group*, 2009a, 2009b, 2010] data sets and binned to the model grid. Γ_{yy} for CFC-11 is formulated as a matrix with nonzero terms on the diagonal elements. The magnitude of the diagonal elements is equivalent to the variance of the observations on the model grid, which is determined by assuming an error of 10% on each individual CFC-11 measurement, which is larger than the analytical error of CFC-11 measurements to take into account the effects of unresolved eddy variability [*Haine and Gray*, 2001]. To this uncertainty, we also add the intra-annual variability of CFC-11 taken from a 1° monthly resolution run of the National Center for Atmospheric Research Community Climate System Model [*Danabasoglu et al.*, 2012] to take into account the fact that intra-annual (seasonal) variability is not captured by the OCIM. Diagonal elements of Γ_{yy} corresponding to years and locations for which there are no CFC-11 measurements are set to a very large number, in order not to affect the solution. Since many (∼80%) of the model grid points have no CFC-11 observations, a weak smoothness constraint (Laplacian-squared term) is also applied which yields nondiagonal elements of Γ_{yy}.

The control parameters of the inverse model $\mathbf{p}$ include the model error terms e_u and e_v and the surface restoring values for temperature, salinity, and Δ^{14}C, as described by *DeVries and Primeau* [2011]. Here the parameter γ, which controls the wind speed dependence of the air-sea CFC-11 flux, is also added to $\mathbf{p}$. The prior expected value of γ, γ_o is set to the OCMIP-2 value of 0.337 h cm^{-1} [*Najjar and Orr*, 1998], with a 30% uncertainty which determines the diagonal elements of Γ_{pp}.

2.3. Control Inversion and Uncertainty Estimation

Prior to the inversion, the OCIM must be initialized with several fixed parameters which are not allowed to vary during the inversion process. These parameters include the isopycnal diffusivity K_I, the vertical diffusivity K_V, and the parameter ω in equation (5), which determines the trade-off between how well the model fits the observations and how large the adjustments to the control parameters are allowed to be. Additional sources of uncertainty include the prior value of the gas exchange coefficient, γ_o, used in the optimization, and uncertainty in the tracer observations to which the model is fit. The "control" inversion (CTL) uses standard values for the isopycnal and diapycnal diffusivities of $K_I = 10^3$ m^2 s^{-1} and $K_V = 10^{-5}$ m^2 s^{-1}, respectively, a value of $\gamma_o = 0.337$ for the gas exchange coefficient [*Najjar and Orr*, 1998], objectively mapped temperature [*Locarnini et al.*, 2010] and salinity [*Antonov et al.*, 2010] fields from the 2009 World Ocean Atlas, objectively mapped natural Δ^{14}C values from GLODAP [*Key et al.*, 2004], CFC-11 observations from the GLODAP and CARINA databases, and a value of $\omega = 3$, which was found to give a good fit to the observations without allowing excessive adjustments to the initial geostrophic momentum balance.

The simulated tracer fields in the CTL model match the observations very well (Figure 2). The largest misfits between modeled and observed tracer distributions are found in the near-surface and thermocline regions. The primary cause of these misfits is most likely the lack of seasonal variability in the model. In order to match the observed tracer distributions in the deeper ocean, the modeled tracer values in the surface mixed layer and upper thermocline are likely closer to winter values than annual mean values, since most deep water formation occurs during the winter. Indeed, near-surface temperatures in the OCIM are much lower than annual mean observed temperatures in those regions where deep water formation occurs, such as the Southern Ocean and North Atlantic. Regionally, the largest model-data misfits occur in the Southern Ocean. In particular, near-surface salinities are higher than observed (annually averaged) salinities; bottom water
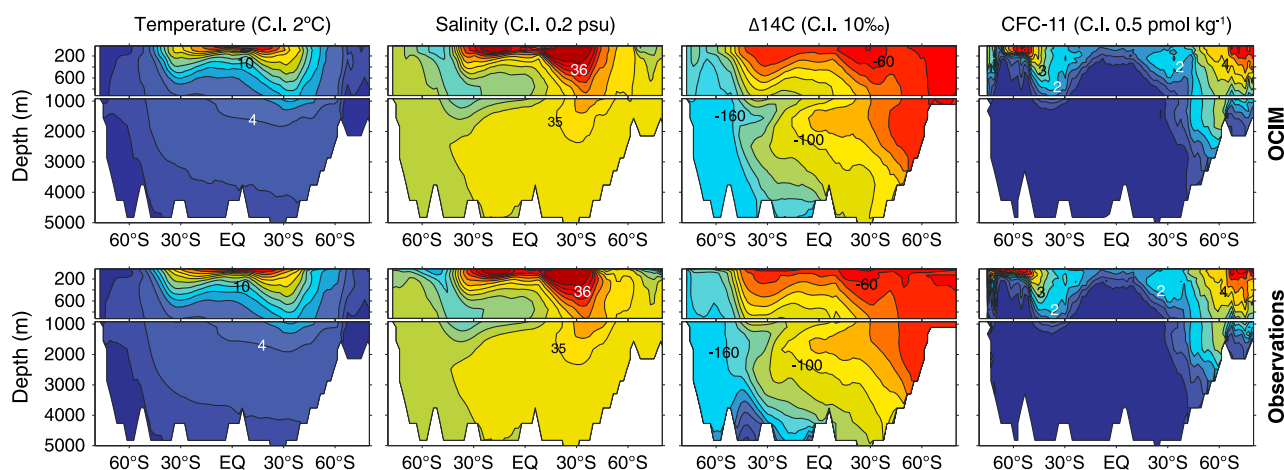
Figure 2. Zonally averaged (top row) modeled and (bottom row) observed tracer distributions in the Atlantic Ocean. Modeled tracer fields from the CTL version of the OCIM. CI: contour interval.

$\Delta^{14}C$ values are higher than observed values, and modeled CFC-11 concentrations are lower than observed in the surface mixed layer south of about 60°S.

To estimate the uncertainty of the OCIM circulation, ventilation, and gas exchange rates, the parameters K_I, K_V, ω, γ_o, and the tracer observations were varied systematically within reasonable bounds in various different configurations of the OCIM (Table 1). The value of ω was varied between $\omega = 2$ (model $\omega2$) and $\omega = 4$ (model $\omega4$) to reflect uncertainty in how much adjustment to the control parameters should be allowed in order to allow the model to fit the observed tracer distributions. The isopycnal diffusivity K_I was set to 600 m² s⁻¹ in model $K_{I,600}$, which is the value used in the Modular Ocean Model version 4p1 (MOM4p1) as implemented in recent earth system model simulations [*Dunne et al.*, 2012]. In model $K_{I,2000}$, the value of K_I was set to 2000 m² s⁻¹ to test the sensitivity of the model to an upper bound estimate of isopycnal diffusivity. Finally, in model $K_{V,1.5}$ the vertical diffusivity was increased by 50% to 1.5×10^{-5} m² s⁻¹, which is the value of K_V used for the high-latitude oceans in MOM4p1 [*Dunne et al.*, 2012]. The gas exchange coefficient γ_o was reduced by 80% from the value in the CTL model to $\gamma_o = 0.27$ cm h⁻¹, consistent with recent estimates based on bomb $\Delta^{14}C$ budgets [*Sweeney et al.*, 2006]. To account for uncertainty in the tracer observations, three additional inversions were run in which noise of the same magnitude as the observational uncertainty was added to the observations (models P1, P2, and P3, Table 1). For the objectively mapped observations (potential temperature, salinity, and $\Delta^{14}C$), spatially correlated noise was added to the data following the procedure described in *DeVries and Primeau* [2011]. For CFC-11, only the raw data were assimilated, and so spatially uncorrelated noise was added to the observations.

Table 2 summarizes the post-optimization performance of the 10 different OCIM configurations in terms of their error statistics. The mean deviation (MD) represents the (volume-weighted) mean difference between

Table 1. The 10 Different Configurations of the OCIM Used in This Study[a]

Model	ω	K_I (m² s⁻¹)	K_V (m² s⁻¹)	γ_o (h cm⁻¹)	Data
CTL	3	1000	10^{-5}	0.337	Observed
$\omega2$	2	1000	10^{-5}	0.337	Observed
$\omega4$	4	1000	10^{-5}	0.337	Observed
$K_{I,2000}$	3	2000	10^{-5}	0.337	Observed
$K_{I,600}$	3	600	10^{-5}	0.337	Observed
$K_{V,1.5}$	3	1000	1.5×10^{-5}	0.337	Observed
$\gamma_{0.27}$	3	1000	10^{-5}	0.27	Observed
P1	3	1000	10^{-5}	0.337	Observed + noise
P2	3	1000	10^{-5}	0.337	Observed + noise
P3	3	1000	10^{-5}	0.337	Observed + noise

[a]See text for details.

Table 2. The Mean Deviation (MD), Root-Mean-Square Error (RMSE), and Relative Error (RE) of Tracer Fields and Selected Model Parameters in Each of the Model Configurations[a]

Model		Temperature (°C)	Salinity (psu)	$\Delta^{14}C$ (‰)	CFC-11 (pmol kg^{-1})	e_u (10^{-6} m s^{-2})	e_v (10^{-6} m s^{-2})	γ (h cm^{-1})
	MD	−0.02	0.001	0.6	−0.02	−0.02	0.01	−0.02
CTL	RMSE	0.37	0.069	6.5	0.24	0.49	0.53	0.08
	RE	0.85	0.79	0.64	1.34	0.82	0.80	0.35
	MD	−0.03	0.001	0.8	−0.03	−0.02	0.01	−0.02
$\omega 2$	RMSE	0.40	0.072	6.9	0.25	0.40	0.42	0.07
	RE	0.91	0.83	0.68	1.41	0.98	0.93	0.45
	MD	−0.02	0.001	0.5	−0.02	−0.02	0.01	−0.02
$\omega 4$	RMSE	0.35	0.067	6.4	0.23	0.57	0.62	0.08
	RE	0.82	0.77	0.62	1.31	0.72	0.72	0.29
	MD	−0.03	0.002	1.2	−0.03	−0.02	0.01	−0.04
$K_{I,2000}$	RMSE	0.37	0.071	7.7	0.25	0.50	0.55	0.10
	RE	0.93	0.84	0.66	1.49	0.82	0.83	0.45
	MD	−0.02	0.001	0.4	−0.02	−0.02	0.01	−0.02
$K_{I,600}$	RMSE	0.37	0.069	6.2	0.23	0.50	0.53	0.07
	RE	0.82	0.78	0.64	1.29	0.84	0.81	0.33
	MD	−0.02	0.001	0.6	−0.02	−0.02	0.01	−0.02
$K_{V,1.5}$	RMSE	0.37	0.069	6.6	0.24	0.49	0.53	0.08
	RE	0.85	0.79	0.64	1.35	0.83	0.81	0.36
	MD	−0.02	0.001	0.6	−0.02	−0.02	0.01	−0.02
$\gamma_{0.27}$	RMSE	0.37	0.069	6.5	0.24	0.49	0.53	0.07
	RE	0.85	0.78	0.64	1.34	0.82	0.80	0.35
	MD	−0.02	0.001	0.8	−0.02	−0.02	0.01	−0.02
P_1	RMSE	0.46	0.082	7.8	0.28	0.51	0.54	0.08
	RE	1.07	1.05	0.71	1.59	0.85	0.83	0.35
	MD	−0.02	0.001	0.7	−0.02	−0.02	0.01	−0.02
P_2	RMSE	0.46	0.082	7.6	0.28	0.51	0.55	0.08
	RE	1.07	1.03	0.70	1.59	0.85	0.83	0.36
	MD	−0.02	0.001	0.8	−0.02	−0.02	0.01	−0.02
P_3	RMSE	0.46	0.082	7.5	0.28	0.51	0.54	0.08
	RE	1.07	1.02	0.71	1.59	0.85	0.83	0.35

[a]The RE is unitless. See text for details and Table 1 for model setup.

the model state and the observations; or in the case of the model parameters, the mean difference between the optimal model parameters and their prior estimated values. The root-mean-square error (RMSE) represents the mean-squared error of the (volume-weighted) deviation between the model state and the observations, or in the case of the model parameters the deviation between the optimal model parameters and their prior estimated values. The relative error (RE) is the square root of the value of that part of the cost function pertaining to each particular model state variable or control parameter.

The relative error of the tracer fields and the model parameters are generally less than 1 for all runs except for those in which noise was added to the observations (models P1, P2, and P3), indicating that the model-data residuals are within the prior expected error bounds. The exception is CFC-11, which has a relative error of between 1.29 and 1.49. This indicates that the 10% prior error that was chosen for CFC-11 is likely too small to fully account for unresolved eddy variability in the model.

The fit between the model and the tracer observations varies substantially over all 10 different OCIM configurations. The best model-data fits are generally found in model $\omega 4$, which is to be expected since that model allows the largest adjustments to the control parameters. Of the models that use the standard value of $\omega = 3$, the model $K_{I,600}$ performs best overall, with the lowest relative error for CFC-11. The $K_{I,2000}$ model performs worst with respect to all tracers, indicating that an isopycnal diffusivity of 2000 m^2 s^{-1} is unrealistically large. The misfit between model and observations increases substantially in the models in which noise
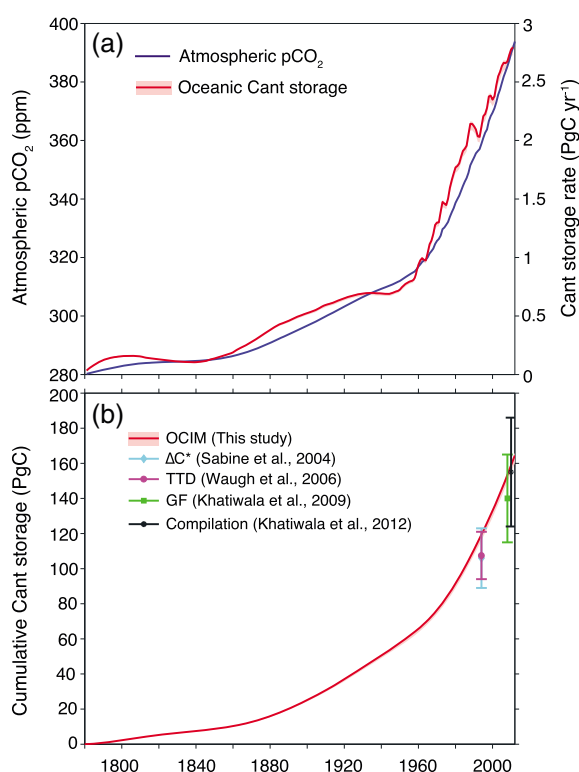
Figure 3. (a) Atmospheric pCO_2 over the industrial era (1780 to present) along with the oceanic anthropogenic CO_2 (C_{ant}) storage rate (light red shading indicates range of model results). Atmospheric pCO_2 is derived from ice core measurements made at Law Dome, Antarctica, for 1780–1958 (available at http://cdiac.ornl.gov/ftp/trends/co2/lawdome.smoothed.yr75) and atmospheric measurements made at Mauna Loa observatory from 1958 to present (available at ftp://ftp.cmdl.noaa.gov/ccg/co2/trends/co2_annmean_mlo.txt). (b) Cumulative C_{ant} storage by the ocean over the industrial era from the ocean circulation inverse model (OCIM, this study, red line plus shading), compared to estimates from the ΔC^* method [*Sabine et al.*, 2004], the TTD method [*Waugh et al.*, 2006], the GF method [*Khatiwala et al.*, 2009], and a compilation of data- and model-based estimates [*Khatiwala et al.*, 2013].

was added to the observations (models P1, P2, and P3). This indicates that the observational fields used in those models are less probable than the standard observational fields used in the other models. This also implies that the model circulation, ventilation, and gas exchange rates in those models are less likely to be correct than those in the models with unperturbed observations.

3. The Oceanic Anthropogenic CO_2 Sink in the OCIM

Anthropogenic CO_2 is simulated using the optimized circulation field and air-sea gas exchange parameter γ from each of the 10 different configurations of the OCIM. The amount of anthropogenic CO_2 in the ocean is estimated as the difference between a time-varying run in which atmospheric pCO_2 increases according to the observed atmospheric history from 1780 to 2012 (Figure 3a), and an initial condition in which the oceanic DIC concentration is in equilibrium with an atmospheric pCO_2 of 280 ppm.

It is assumed that biological processes in the ocean are not affected by the rising atmospheric CO_2 concentration so that biological sources and sinks of DIC can be neglected. In this case, sources and sinks of CO_2 are driven only by gas exchange, as parameterized by equations (3) and (4) with **c** the concentration of dissolved CO_2 gas in seawater. The solubility of CO_2 in seawater depends on the sea surface temperature and salinity, which is assumed to be constant over the industrial period. The speciation of DIC into carbonate species and dissolved CO_2 also depends on the seawater alkalinity, which is similarly taken to be a constant salinity-normalized value over the industrial period. Therefore, any changes in CO_2 uptake over the industrial era that have been driven by changes in seawater temperature, salinity, or alkalinity (i.e., changes in the solubility pump) are not accounted for in this calculation. Model simulations have shown that changes in the solubility pump have only a very small effect on the oceanic uptake of anthropogenic CO_2 [*Wang et al.*, 2012], justifying their neglect here.

3.1. Global Ocean Storage of Anthropogenic CO_2

Results from the OCIM show that the oceanic storage rate of C_{ant} (obtained by centered differences of the oceanic C_{ant} storage) increases along with atmospheric pCO_2 throughout the industrial era (Figure 3a). The increase in oceanic C_{ant} storage rate is not monotonic, due to fluctuations in the atmospheric pCO_2 growth rate. Note that interannual variability due to variability in ocean circulation, which is ~0.2–0.4 PgC yr^{-1} [*Wanninkhof et al.*, 2013], is not represented in the OCIM-estimated C_{ant} storage rates. Averaged over the period 2000–2010, the oceanic C_{ant} storage rate is about 2.6 PgC yr^{-1}, while carbon emissions from fossil fuel burning, cement production, and gas flaring averaged to 8.1 PgC yr^{-1} over the same period [*Boden et al.*, 2013]. The contemporary oceanic C_{ant} sink thus represents about 30% of current fossil fuel CO_2 emissions.

Cumulative oceanic C_{ant} storage in 2012 ranges from 160 to 166 PgC over the 10 different OCIM configurations, with a mean C_{ant} storage of 164 PgC (Figure 3b). The estimate from the OCIM is larger than the corresponding estimates from the ΔC^* and TTD estimates for 1994, the nominal year to which those estimates apply (Figure 3b). A portion of this discrepancy can be attributed to the additional areas covered by the OCIM estimate, including the Arctic Ocean and Mediterranean Sea, which together stored about 4 PgC in 1994. The OCIM C_{ant} estimate is within the uncertainty of the C_{ant} estimates from the GF approach [*Khatiwala et al.*, 2009], which also did not include the Arctic Ocean and Mediterranean Sea. *Khatiwala et al.* [2013] used a compilation of data- and model-based estimates to derive a "best guess" estimate of 155±35 PgC of oceanic C_{ant} storage for the year 2010. The OCIM estimate of 155–160 PgC for 2010 lies very close to the mean of this estimate. C_{ant} storage by the ocean in 2010 amounted to approximately 42–44% of the cumulative fossil fuel carbon emissions over the industrial era of ∼365 PgC [*Boden et al.*, 2013].

The uncertainty on the OCIM C_{ant} storage estimates for the global ocean is quite small (∼3 PgC or 2% of the global C_{ant} inventory in 2012), despite significant differences among the 10 different versions of the OCIM in terms of the underlying model parameters (see Table 1). There are several reasons for this. In the OCIM, the application of tracer constraints on the ocean circulation greatly reduces the sensitivity of the circulation and ventilation rates (and associated C_{ant} uptake) to the values of the isopycnal and vertical diffusivities. This is because in the OCIM, the momentum balance can be adjusted locally to overcome deficiencies in the subgridscale diffusivity parameterization that might cause discrepancies between the modeled and observed tracer fields. This contrasts with OGCMs that are not constrained by observations, which show a strong sensitivity of C_{ant} uptake to variations in diffusivities [e.g., *Mikaloff-Fletcher et al.*, 2006]. Similarly, uncertainty in the observations translates to only small uncertainty in the OCIM-estimated C_{ant} sink due to prior constraints placed on the magnitude of the model error terms, such that the adjustments to the momentum balance have to occur within reasonable bounds [*DeVries and Primeau*, 2011]. This effectively penalizes "unrealistic" observations. Thus, the combination of dynamical and observational constraints on the circulation of the OCIM reduces the uncertainty on C_{ant} uptake compared to estimates that apply primarily observational constraints [e.g., *Sabine et al.*, 2004; *Waugh et al.*, 2006; *Khatiwala et al.*, 2009] or OGCM-based estimates that apply primarily dynamical ocean circulation constraints [e.g., *Mikaloff-Fletcher et al.*, 2006].

The C_{ant} uptake is relatively insensitive to the value of the initial air-sea gas exchange rate γ_o used in the OCIM. In the CTL run, with $\gamma_o = 0.337$, the oceanic C_{ant} storage in 2012 is 165 PgC, while in the $\gamma_{0.27}$ run, the oceanic C_{ant} storage in 2012 is 161 PgC. This is partly due to the fact that the optimal value of γ is adjusted at each surface grid point to achieve consistency with the observed CFC-11 concentration, but more so to the fact that surface-to-deep ocean ventilation rates, and not air-sea gas exchange rates, are the rate-limiting step in oceanic CO_2 uptake [*Sarmiento et al.*, 1992; *Graven et al.*, 2012]. The models that use a value of $\gamma_o = 0.337$ converge to a slightly lower global mean value of about $\gamma = 0.31$. Almost all adjustment occurs in the Southern Ocean south of 40°S, where the mean value of $\gamma = 0.24$. However, it appears that the actual value of γ is not that well constrained by the CFC-11 observations, as the value of γ in the Southern Ocean in model $\gamma_{0.27}$ is even lower at $\gamma = 0.18$. Information from additional tracers, such as bomb-produced $\Delta^{14}C$, is needed to better constrain the magnitude and spatial variability in γ.

Although the uncertainty on globally integrated C_{ant} storage in the OCIM is small, the uncertainty on C_{ant} concentrations at smaller spatial scales can be substantial. At the grid scale, the global average uncertainty on C_{ant} concentrations in 2012 is ±2.9 μmol kg^{-1}, taking the full range of model results as a measure of uncertainty. Maximum differences in oceanic C_{ant} concentrations between the 10 different versions of the OCIM can exceed 30 μmol kg^{-1} at the grid scale. However, these errors largely cancel out upon integrating over large areas.

Several potentially important sources of uncertainty are not accounted for in these calculations. These include potential biases in the model due to structural errors in the model circulation, for example due to unresolved seasonality or to unresolved subgridscale flows. The assimilation of tracer data reduces these structural errors to a minimum relative to other models of similar resolution, but some biases may still remain as evidenced for example by model-data misfits in the Southern Ocean (Figure 2). Other potentially important sources of error include biases due to the assumptions of steady state ocean circulation and biology. All of these potential structural biases and assumptions are also inherent in previous approaches to resolve the temporal variability in global ocean CO_2 storage from observations [e.g., *Khatiwala et al.*, 2009], and so the uncertainties reported here are directly comparable to uncertainties reported in those studies.
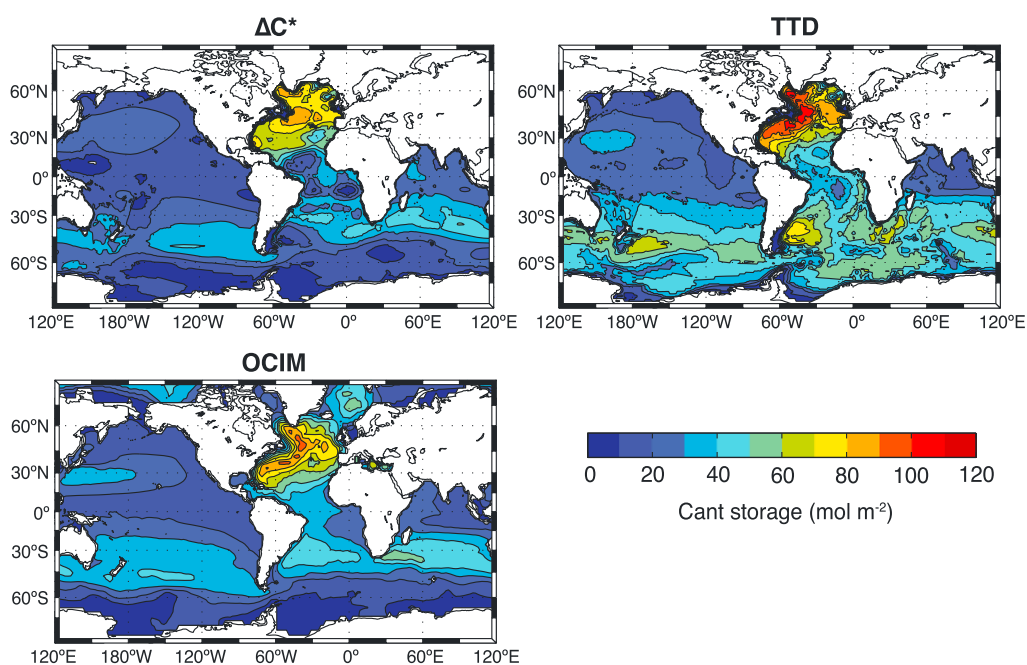
Figure 4. Depth-integrated oceanic C_{ant} storage for the reference year 1994 for three different data-based estimates using the ΔC^* method [*Sabine et al.*, 2004], the TTD method [*Waugh et al.*, 2006], and the OCIM (this study). No corrections to the ΔC^* or TTD results have been applied. (In the original studies, negative values were removed from the ΔC^* C_{ant} estimates [*Sabine et al.*, 2004], and the TTD C_{ant} concentrations were reduced by 20% uniformly [*Waugh et al.*, 2006].) Contour interval is 10 mol m^{-2}.

Perhaps the largest source of "unestimated" error in the OCIM C_{ant} calculations results from the assumption of a constant ocean circulation over the industrial era. Analysis of repeated CFC observations in the Southern Ocean have shown substantial changes in the circulation and ventilation in that region over the last several decades, with potentially important implications for the oceanic CO_2 sink [*Waugh et al.*, 2013]. Simulations of CO_2 uptake in OGCMs driven with time-varying surface forcing generally show a substantial slowdown in the rate of increase in oceanic CO_2 uptake since the 1990s [*Sarmiento et al.*, 2010; *Wanninkhof et al.*, 2013], which has been attributed primarily to increased outgassing of "natural" CO_2 (stored since preindustrial times) from the Southern Ocean [*Lovenduski et al.*, 2008]. A rough estimate of the magnitude of this effect can be obtained by comparing the pre- and post-1990 CO_2 sinks in the OCIM with those in OGCMs with time-varying forcing. *Sarmiento et al.* [2010] found a net oceanic CO_2 sink of 1.46 ± 0.27 PgC yr^{-1} from 1960 to 1988, consistent with the OCIM estimate of 1.47 ± 0.02 PgC yr^{-1} for the same time period. However, from 1989 to the mid-2000s, *Sarmiento et al.* [2010] found a net oceanic CO_2 sink of 1.97 ± 0.25 PgC yr^{-1} (0.51 PgC yr^{-1} larger than for 1960–1988), while the OCIM CO_2 sink is 2.29 ± 0.02 PgC yr^{-1} for the period 1989–2005 (0.82 PgC yr^{-1} larger than for 1960–1988). This could indicate that the OCIM C_{ant} uptake post-1989 is about 0.31 PgC yr^{-1} (0.82 − 0.51) too high (in other words, it does not account for an additional 0.31 PgC yr^{-1} efflux of natural CO_2 from the ocean to the atmosphere). If net oceanic CO_2 uptake were decreased by 0.31 PgC yr^{-1} after 1989, it would translate to a reduction in oceanic CO_2 storage of about 7 PgC in the year 2012 or slightly less than 5% of the global oceanic C_{ant} inventory.

3.2. Regional Storage, Air-Sea Fluxes, and Transports of Anthropogenic CO_2

The regional distribution of C_{ant} storage in the ocean estimated from the OCIM differs substantially from previous data-based estimates. Figures 4 and 5 compare C_{ant} estimates from the OCIM with estimates from the ΔC^* and TTD methods for the reference year 1994. C_{ant} storage estimates from the GF method are not shown, as those estimates are not publicly available; however, comparisons can be made over some broad regions tabulated in *Wang et al.* [2012, Table 2] and with the depth-integrated C_{ant} storage for 2008 shown in *Khatiwala et al.* [2009, Figure 1a].

The highest concentrations of C_{ant} in all the data-based estimates occur in the North Atlantic. The OCIM estimate shows that C_{ant} storage is concentrated along the pathway of the deep western boundary current in
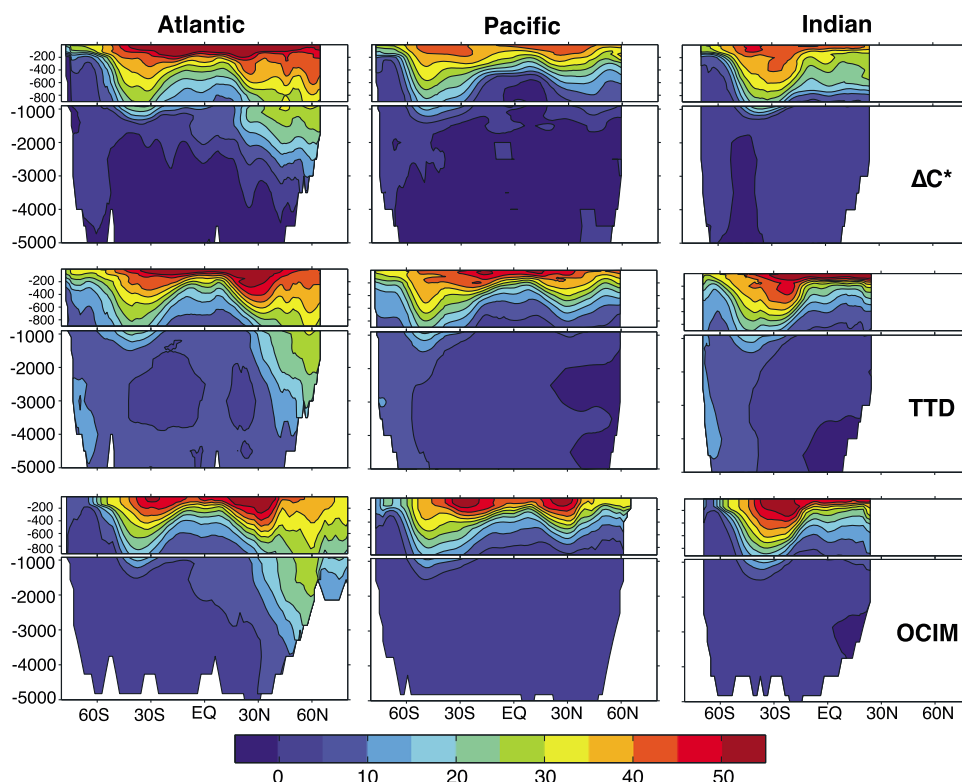
Figure 5. Zonally integrated sections of oceanic C_{ant} storage for the reference year 1994 for (left column) the Atlantic Ocean, (middle column) the Pacific Ocean, and (right column) the Indian Ocean using (top row) the ΔC* method [*Sabine et al.*, 2004], (middle row) the TTD method [*Waugh et al.*, 2006], and (bottom row) the OCIM (this study). Contour interval is 5 μmol kg^{-1}.

the North Atlantic. The distribution of C_{ant} in the North Atlantic inferred by the ΔC* and TTD estimates are more diffuse in the east-west direction, with stronger north-south gradients (Figure 4). When compared with the GF estimate [*Khatiwala et al.*, 2009, Figure 1a], the OCIM estimate shows much higher C_{ant} concentrations in the western North Atlantic south of about 45°S, associated with a better representation of the western boundary currents. The depth distribution of C_{ant} in the OCIM better resembles the TTD-based rather than the ΔC*-based C_{ant} estimates, with greater accumulation of C_{ant} in the deep ocean and lesser C_{ant} accumulation at shallow depths (Figure 5). This is in agreement with *Matsumoto and Gruber* [2005], who found that the ΔC* method overpredicts C_{ant} concentrations in the thermocline but underpredicts C_{ant} concentrations at depth. The total storage in the North Atlantic (between the equator and 60°N) is similar in all four data-based estimates: 22 PgC in the ΔC* and GF estimates and 25 PgC in the TTD and OCIM estimates.

Substantial differences among the data-based C_{ant} estimates also occur in the Southern Ocean (south of 35°S). The OCIM estimate is in much better agreement with the ΔC* estimate, both in terms of pattern and magnitude, than the TTD estimate (Figure 4). The TTD C_{ant} storage is too high in the Southern Ocean, partly due to the incorrect assumption of constant air-sea CO_2 disequilibrium in this method [*Waugh et al.*, 2006]. The OCIM estimate yields 30 PgC C_{ant} stored in the Southern Ocean, similar to the 27 PgC estimated by the ΔC* method, but much smaller than the 50 PgC estimated by the TTD method and also smaller than the 36 PgC estimated by the GF method [*Khatiwala et al.*, 2009; *Wang et al.*, 2012]. In terms of the C_{ant} depth distribution, the OCIM shows less C_{ant} storage in the upper ocean south of 60°S than the ΔC* and TTD methods (Figure 5). This is in spite of strong C_{ant} uptake in this region, indicating strong northward C_{ant} transport (see below).

The third most important region for oceanic C_{ant} storage is the North Pacific (Figures 4 and 5). Here the OCIM C_{ant} storage estimate of 19 PgC is in better agreement with the estimate from the TTD method (20 PgC) and the GF method (18 PgC) [*Wang et al.*, 2012] than the ΔC* estimate (14 PgC). Both the OCIM and TTD estimates show preferential C_{ant} storage in the western North Pacific, presumably associated with North Pacific
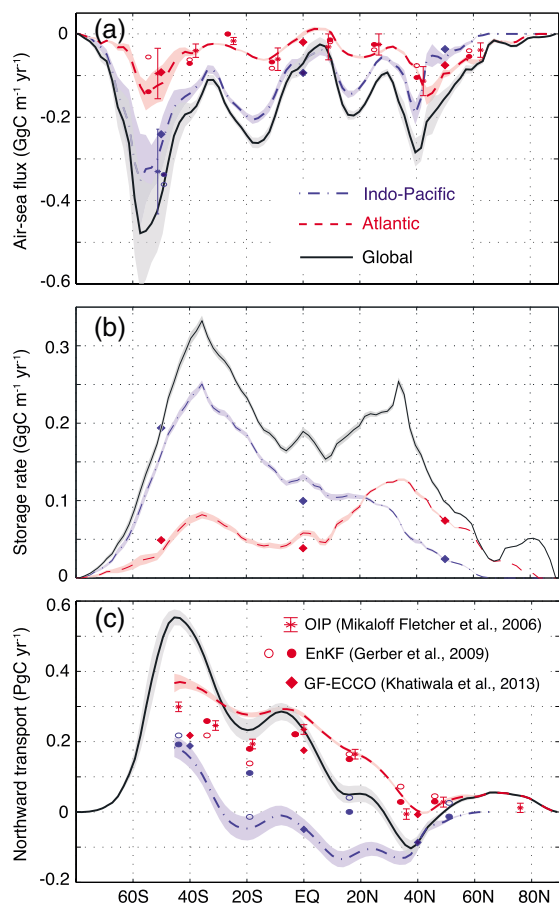
Figure 6. Zonally integrated (a) air-sea anthropogenic CO$_2$ flux, (b) anthropogenic CO$_2$ storage rate, and (c) northward anthropogenic CO$_2$ transport from the OCIM in the Atlantic (dashed red curves), Indo-Pacific (dot-dashed blue curves), and global oceans (solid black curves) for the year 2012. Shading represents the 1σ uncertainty envelope from the ensemble of OCIM runs. Also shown in Figures 6a–6c are corresponding estimates derived from assimilating data-based anthropogenic CO$_2$ estimates into OGCMs [*Mikaloff-Fletcher et al.*, 2006; *Gerber et al.*, 2009] (OIP and EnKF) and from the GF approach of *Khatiwala et al.* [2013] (GF-ECCO). Red symbols correspond to estimates for the Atlantic Ocean, and blue symbols to estimates for the Indo-Pacific Oceans (for EnKF and GF-ECCO estimates only). For the EnKF estimates [*Gerber et al.*, 2009], ΔC*-based estimates are shown as open circles, and TTD-based estimates are shown as closed circles. All estimates are scaled to the year 2012.

Intermediate Water formation, which is not resolved to as great a degree in the ΔC* estimate. Preferential C$_{ant}$ storage in the western North Pacific is also not captured by the GF method to the degree that it is in the OCIM [c.f. *Khatiwala et al.*, 2009, Figure 1a].

Accounting for dynamical ocean circulation constraints in the inversion generates a physically more realistic pattern of oceanic C$_{ant}$ storage. This can be seen for example in the concentration of C$_{ant}$ along the deep western boundary current in the North Atlantic of the OCIM (Figure 4) and in the resolution of significant zonal and meridional gradients in C$_{ant}$ storage in the subtropical and tropical oceans, associated with upwelling along eastern boundaries and near the equator (Figures 4 and 5). Uncertainties in the vertically integrated C$_{ant}$ storage in 1994 average about 3 mol m^{-2}, with largest uncertainties (>5 mol m^{-2}) in the Southern Ocean-Drake Passage region and the western North Atlantic.

The OCIM-estimated air-sea fluxes, storage rates, and transport rates can be compared with results from previous inverse modeling studies by scaling the previous estimates to the year 2012 (Figure 6). This was done by assuming that the proportional change in C$_{ant}$ air-sea fluxes (or storage rates or transport rates) between the year in which the estimate is provided and the year 2012 is equivalent in both the OCIM and the previous estimates. These previous estimates include the Ocean Inversion Project (OIP), in which air-sea fluxes in a suite of 10 OGCMs were adjusted to achieve an optimal fit to ΔC*-based C$_{ant}$ estimates [*Mikaloff-Fletcher et al.*, 2006, Table 2 and Figure 5], an ensemble Kalman filter (EnKF) approach in which ΔC*- and TTD-based C$_{ant}$ estimates (as well as C$_{ant}$ estimates from several other less accurate methods not considered here) were assimilated into a coarse-resolution OGCM, again by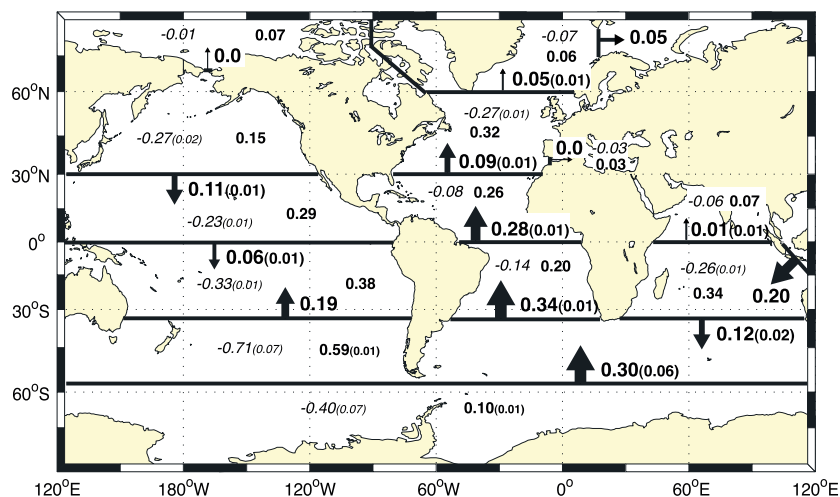 adjusting air-sea fluxes [*Gerber et al.*, 2009, Tables 2 and 4], and a study in which the GF approach, along with transport information from the ECCO OGCM, was used to derive air-sea fluxes and depth-integrated storage rates for 26 large ocean patches [*Khatiwala et al.*, 2013, Figure 6].

The air-sea flux of C$_{ant}$ in the OCIM shows a strong peak in the Southern Ocean, consistent with previous estimates (Figure 6a). In this region, C$_{ant}$ uptake is high due to strong winds and high CO$_2$ solubilities and due to continual upwelling of old, C$_{ant}$-poor waters. C$_{ant}$ uptake is also strong in the northern high latitudes, where it peaks at about 40°N, and in the tropics at about 20°N and S. Interestingly, there is net outgassing of C$_{ant}$ at the equator in the Atlantic Ocean, due to the accumulation of C$_{ant}$ in surface waters there (see Figure 5). The uncertainties on air-sea fluxes in the OCIM are reduced compared to the OIP and EnKF estimates [*Mikaloff-Fletcher et al.*, 2006], due to the additional circulation constraints provided by the tracer

Figure 7. Air-sea fluxes, storage rates, and transports of anthropogenic CO_2 (in PgC yr^{-1}) from the OCIM for 13 ocean regions for the year 2012. Air-sea fluxes (negative values are into the ocean) are in small italic numbers, storage rates are in small bold numbers, and transports are in large bold numbers. Uncertainties (in parentheses) are only shown if they are at least 0.01 PgC yr^{-1}. Arrows indicate the direction of transport, and the size of the arrows scales approximately with the magnitude of the transport. Budgets in each region may not completely balance due to rounding errors.

observations assimilated in the OCIM. Uncertainties have not been estimated for the GF-ECCO approach. OCIM-estimated uncertainties on air-sea fluxes are minimal in the tropical and subtropical regions, while uncertainties are largest in the Southern Ocean (Figure 6a).

Globally, C_{ant} storage rates are highest in the midlatitudes, particularly the sub-Antarctic region of the Pacific and Indian Oceans (Figure 6b). A secondary maximum in the storage rate is found in the midlatitude North Atlantic Ocean, due to convergence of C_{ant} flowing northward with Antarctic Intermediate Water and southward with North Atlantic Deep Water. The latitudinal distribution of C_{ant} storage rate in the OCIM is similar to that derived from the GF-ECCO method [*Khatiwala et al.*, 2013] although the OCIM estimates a slightly lower storage rate in the Southern Ocean and higher storage rate in the equatorial oceans (Figure 6b).

Overall, there is a strong northward transport of C_{ant} throughout the Southern Hemisphere (peaking at about 0.55 PgG yr^{-1} near 45°S), and northward C_{ant} transport continues across the equator well into the Northern Hemisphere (Figure 6c). The net global northward C_{ant} transport is driven primarily by the Atlantic Ocean, where transport is northward across all latitudes. Northward C_{ant} transports in the South Atlantic in the OCIM are larger than those predicted by the OIP, EnKF, or GF-ECCO approaches. In the Indo-Pacific basin, C_{ant} is primarily transported southward except south of about 30°S (Figure 6c), in good agreement with the GF-ECCO-predicted transport rates but substantially different from those predicted by the EnKF approach.

The large-scale contemporary oceanic C_{ant} sink estimated from the OCIM is summarized in Figure 7. The Southern Ocean (south of 35°S) experiences the largest net air-sea flux of anthropogenic CO_2, currently taking up about 1.1 PgC yr^{-1} or about 40% of the global oceanic C_{ant} uptake. The Antarctic region of the Southern Ocean (south of 55°S) stores only about 25% of the C_{ant} that it absorbs from the atmosphere—the remainder is transported northward into the sub-Antarctic zone, where it is either stored or is transported farther northward into the tropical and subtropical Atlantic and Pacific Oceans (Figure 7). The North Pacific Ocean (north of the equator) also takes up a substantial amount of CO_2 on the order of 0.5 PgC yr^{-1}, most of which is stored locally but some of which is transported across the equator. The South Pacific Ocean experiences a net convergence of C_{ant} transported from the North Pacific and from the Southern Ocean, not only contributing to substantial C_{ant} storage in this region but also leading to a large transport of C_{ant} into the southern Indian Ocean through the Indonesian Throughflow (ITF) (Figure 7). A loop connecting the Southern Ocean, South Pacific, and South Indian Oceans can be identified in which C_{ant} is taken up in the Southern Ocean, transported northward into the South Pacific, then transported laterally through the ITF into the South Indian, and ultimately transported southward into the Southern Ocean once more (Figure 7).
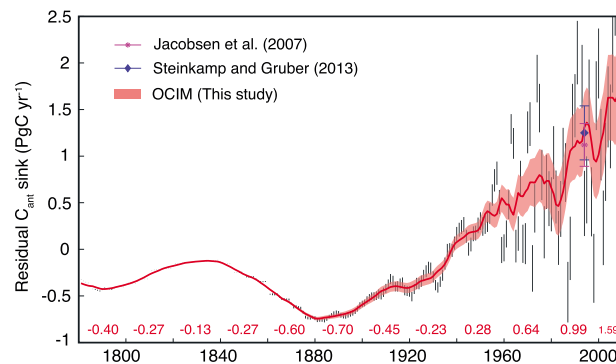
Figure 8. The residual sink (RS; positive values indicate a flux of CO_2 out of the atmosphere) of anthropogenic CO_2 in the OCIM. Black lines represent the annual RS which is derived from centered differencing of the cumulative residual sink (equation (6)). The range of values at each year includes error due to the range of oceanic C_{ant} storage derived from the 10 different versions of the OCIM and 10% error on cumulative CO_2 emissions [*Andres et al.*, 2012]. The red line (with 1σ uncertainty shading) is the 5 year running mean of the annual RS. Also shown are estimates of the terrestrial CO_2 sink for the period 1992–1996 from *Jacobson et al.* [2007] and *Steinkamp and Gruber* [2013]. Numbers in red (at bottom) represent the average RS for each 20 year time interval graded on the *x* axis (the number at the bottom right is for the interval 2000–2010).

4. Implications for the Terrestrial Sink of Anthropogenic CO_2

A cumulative residual source or sink (CRS) of anthropogenic CO_2 can be inferred from the difference between cumulative anthropogenic CO_2 emissions (C_{ant}^{em}) and C_{ant} accumulated in the atmosphere (C_{ant}^{atm}) and in the ocean (C_{ant}^{oce})

$$CRS = C_{ant}^{em}(t) - C_{ant}^{atm}(t) - C_{ant}^{oce}(t). \quad (6)$$

Here $C_{ant}^{em}(t)$ is the cumulative amount of anthropogenic CO_2 emissions at time *t* due to fossil fuel burning, cement production, and gas flaring [*Boden et al.*, 2013], C_{ant}^{atm} is the difference between the amount of C in the atmosphere at time *t* and that in year 1780, and $C_{ant}^{oce}(t)$ is the amount of C_{ant} stored in the ocean, estimated from the OCIM.

The CRS of C_{ant} calculated in this way can be interpreted as representing a cumulative terrestrial source or sink of anthropogenic CO_2, with some caveats. First, the CRS includes not only C_{ant} stored in the terrestrial biosphere but could also include C_{ant} stored in inland waters, estuaries, coastal marine sediments, and C_{ant} transported laterally from land to the open ocean [*Regnier et al.*, 2013]. Second, a portion of the CRS may also reflect changes in the fluxes of "natural" CO_2, i.e., CO_2 fluxes that are not driven by human activity, including variability in the air-sea flux of natural CO_2 that is not accounted for by the steady-state OCIM. Third, the CRS inherits any interannual variability in the oceanic C_{ant} sink which is not represented in the OCIM; however, the interannual variability in oceanic CO_2 uptake is small compared to the interannual variability in the terrestrial CO_2 sink [*Sarmiento et al.*, 2010].

The year-to-year change in the CRS, which is referred to here as the residual sink (RS), primarily reflects changes in the terrestrial flux of CO_2 (Figure 8). Interannual variability in the RS is very large, which reflects short-term climate variability such as the effects of El Niño–Southern Oscillation and major volcanic eruptions [*Sarmiento et al.*, 2010]. This interannual variability is effectively filtered out by applying a 5 year running mean filter to the results (Figure 8, red curve). The RS is negative from the beginning of the industrial era up to about 1940, which is consistent with a large net flux of CO_2 from terrestrial ecosystems due to deforestation and land use changes [*Houghton*, 2003]. From 1940 onward the RS is positive and generally increasing over time, due to various factors including afforestation and the fertilizing effects of CO_2 and anthropogenic nitrate emissions on the terrestrial biosphere [*Canadell et al.*, 2007], while land use change continues to constitute a net source of CO_2 to the atmosphere [*Houghton et al.*, 2012]. A large sink of C in world's forests (1.1 ± 0.8 PgC yr^{-1}) over the last several decades [*Pan et al.*, 2011] may account for most of the 1.38 ± 0.20 PgC yr^{-1} RS in the OCIM over that period.

The RS estimated from the OCIM generally agrees with the RS estimates from other modeling studies. For the period 1960–1988, the RS estimated from the OCIM is 0.56 ± 0.13 PgC yr^{-1}, which is higher than the RS estimated by *Sarmiento et al.* [2010], who calculated an RS of 0.27 ± 0.27 for the same period. Since the oceanic CO_2 uptake in the OCIM and in the ocean models analyzed by *Sarmiento et al.* [2010] are nearly identical for that period, the difference between the RS of the two estimates is attributed to differences in the emission data used in both studies. Leaving out emissions from cement production and gas flaring, and using only fossil fuel emissions as in *Sarmiento et al.* [2010], yields a RS of 0.37 ± 0.12 for the period 1960–1988 in the OCIM, in much better agreement with the results of *Sarmiento et al.* [2010]. For the period 1989–2005, the OCIM RS is 1.24 ± 0.20 PgC yr^{-1} (0.97 ± 0.19 using only fossil fuel emissions), in agreement

with the RS of 1.15±0.23 estimated by *Sarmiento et al.* [2010] for the same period. The OCIM RS for the 1990s is 1.16±0.19 PgC yr^{-1}, which is also in agreement with other independent estimates of the terrestrial CO_2 sink. The joint ocean-atmosphere inversions of *Jacobson et al.* [2007] and *Steinkamp and Gruber* [2013] estimated a terrestrial CO_2 sink of 1.12±0.23 PgC yr^{-1} and 1.25±0.29 PgC yr^{-1}, respectively, for the period 1992–1996. The contemporary RS in the OCIM is 1.59±0.24 PgC yr^{-1} over the period 2000–2010. As noted by *Regnier et al.* [2013], approximately 0.5 PgC yr^{-1} of the contemporary terrestrial C sink is actually stored in coastal and estuarine sediments, and perhaps, 0.1 PgC yr^{-1} is rerouted to the open ocean, leaving about 1.0 PgC yr^{-1} stored in the terrestrial biosphere.

5. Conclusions

This study presented a new estimate of the oceanic anthropogenic CO_2 (C_{ant}) sink, obtained by assimilating multiple tracers (temperature, salinity, radiocarbon, and CFC-11) into an Ocean Circulation Inverse Model (OCIM). The simultaneous application of both observational and dynamical constraints in the OCIM was able to reduce uncertainties in the oceanic C_{ant} sink when compared with other purely data-based or model-based approaches. While the OCIM-estimated oceanic C_{ant} sink shows improved accuracy and precision compared to previous estimates, significant sources of uncertainty remain, primarily due to potential variability in the ocean circulation and the biological pump over the industrial era which is not accounted for in the OCIM.

In particular, oceanographic observations indicate that the circulation of the Southern Ocean may have undergone substantial changes in the last decade or two, presumably in response to the formation of the Antarctic zone hole and associated changes in the Southern Hemisphere westerly winds [*Waugh et al.*, 2013]. Inversions of atmospheric data [*Le Quéré et al.*, 2007] and OGCM simulations [e.g., *Lovenduski et al.*, 2008] suggest that such circulation changes may have weakened the Southern Ocean CO_2 sink. A high priority should be put on developing data-based estimates of the oceanic C_{ant} sink that address the issue of ocean circulation variability more explicitly, focusing particularly on changes in the Southern Ocean, which is the largest regional anthropogenic CO_2 sink.

How the ocean's biological carbon pump has responded to climate variability over the industrial era is an open question. Some studies have suggested that increasing CO_2 concentrations may have a fertilizing effect on marine biota, leading to a stronger biological pump [e.g., *Riebesell et al.*, 2007]. However, at the same time, increased ocean acidification may impair the ability of calcifying organisms to create $CaCO_3$ tests, leading to a weaker biological pump by the reduction of mineral ballast [*Hofmann and Shellnhuber*, 2009]. The net impact of all of these effects on the ocean's biological pump is unclear at this time, and whether there has been any significant effect on the oceanic C_{ant} sink is not known. It will be important to resolve these issues in order to develop more confident estimates of changes in the oceanic anthropogenic CO_2 sink.

References

Andres, R. J., et al. (2012), A synthesis of carbon dioxide emissions from fossil-fuel combustion, *Biogeosciences*, *9*, 1845–1871.
Antonov, J. I., et al. (2010), World Ocean Atlas 2009, Volume 2: Salinity, in *NOAA Atlas NESDIS 69*, edited by S. Levitus, U. S. Government Printing Office, Washington, D. C.
Bates, N. R., M. H. P. Best, K. Neely, R. Garley, A. G. Dickson, and R. J. Johnson (2012), Detecting anthropogenic carbon dioxide uptake and ocean acidification in the North Atlantic Ocean, *Biogeosciences*, *9*, 2509–2522.
Boden, T., B. Andres, and G. Marland (2013), *Global CO₂ Emissions From Fossil-Fuel Burning, Cement Manufacture, and Gas Flaring: 1751–2010*, Carbon Dioxide Information Analysis Center, Oak Ridge National Laboratory, U. S. Department of Energy, Oak Ridge, Tenn.
Bullister, J. L. (2011), *Atmospheric CFC-11, CFC-12, CFC-113, CCl4 and SF6 Histories*, Carbon Dioxide Information Analysis Center, Oak Ridge National Laboratory, U. S. Department of Energy, Oak Ridge, Tenn.
Canadell, J. G., D. E. Pataki, R. Gifford, R. A. Houghton, Y. Luo, M. R. Raupach, P. Smith, and W. Steffen (2007), Saturation of the terrestrial carbon sink, in *Terrestrial Ecosystems in a Changing World*, edited by J. G. Canadell, D. Pataki, and L. Pitelka, Springer-Verlag, Berlin, Germany.
Carbon In The Atlantic Ocean Group (2009a), *Carbon in the Atlantic Ocean Region—The CARINA Project: Results and Data, Version 1.0.*, Carbon Dioxide Information Analysis Center, Oak Ridge National Laboratory, U. S. Department of Energy, Oak Ridge, Tenn.
Carbon In The Atlantic Ocean Group (2009b), *Carbon in The Arctic Mediterranean Seas Region—The CARINA Project: Results and Data, Version 1.2*, Carbon Dioxide Information Analysis Center, Oak Ridge National Laboratory, U. S. Department of Energy, Oak Ridge, Tenn.
Carbon In The Atlantic Ocean Group (2010), *Carbon in the Southern Ocean Region–The CARINA Project: Results and Data, Version 1.1*, Carbon Dioxide Information Analysis Center, Oak Ridge National Laboratory, U. S. Department of Energy, Oak Ridge, Tenn.
Ciais, P., et al. (2013), Carbon and other biogeochemical cycles, in *Climate Change 2013: The Physical Science Basis. Contribution of Working Group I to the Fifth Assessment Report of the Intergovernmental Panel on Climate Change*, edited by T. F. Stocker et al., Cambridge Univ. Press, Cambridge, U. K., and New York.

Danabasoglu, G., S. C. Bates, B. P. Briegleb, S. R. Jayne, M. Jochum, W. G. Large, S. Peacock, and S. G. Yeager (2012), The CCSM4 ocean component, *J. Clim.*, *25*, 1361–1389.

de Boyer Montégut, C., G. Madec, A. S. Fischer, A. Lazar, and D. Iudicone (2004), Mixed layer depth over the global ocean: An examination of profile data and a profile-based climatology, *J. Geophys. Res.*, *109*, C12003, doi:10.1029/2004JC002378.

DeVries, T., and F. Primeau (2011), Dynamically- and observationally-constrained estimates of water-mass distributions and ages in the global ocean, *J. Phys. Oceanogr.*, *41*, 2381–2401, doi:10.1175/JPO-D-10-05011.1.

DeVries, T., C. Deutsch, F. Primeau, B. Chang, and A. Devol (2012a), Global rates of water-column denitrification derived from nitrogen gas measurements, *Nat. Geosci.*, *5*(8), 547–550.

DeVries, T., F. Primeau, and C. Deutsch (2012b), The sequestration efficiency of the biological pump, *Geophys. Res. Lett.*, *39*, L13601, doi:10.1029/2012GL051963.

DeVries, T., C. Deutsch, P. Rafter, and F. Primeau (2013), Marine denitrification rates determined from a global 3-dimensional inverse model, *Biogeosciences*, *9*, 14,013–14,052.

Dunne, J. P., et al. (2012), GFDL's ESM2 Global Coupled Climate-Carbon Earth System Models. Part I: Physical formulation and baseline simulation characteristics, *J. Clim.*, *25*, 6646–6665.

England, M. H., and E. Maier-Reimer (2001), Using chemical tracers to assess ocean models, *Rev. Geophys.*, *39*, 29–70.

Gerber, M., and F. Joos (2010), Carbon sources and sinks from an Ensemble Kalman Filter ocean data assimilation, *Global Biogeochem. Cycles*, *24*, GB3004, doi:10.1029/2009GB003531.

Gerber, M., and F. Joos (2013), An Ensemble Kalman Filter multi-tracer assimilation: Determining uncertain ocean model parameters for improved climate-carbon cycle projections, *Ocean Modell.*, *64*, 29–45.

Gerber, M., F. Joos, M. Vazquez-Rodriguez, F. Touratier, and C. Goyet (2009), Regional air-sea fluxes of anthropogenic carbon inferred with an Ensemble Kalman Filter, *Global Biogeochem. Cycles*, *23*, GB1013, doi:10.1029/2008GB003247.

Graven, H. D., N. Gruber, R. Key, S. Khatiwala, and X. Giraud (2012), Changing controls on oceanic radiocarbon: New insights on shallow-to-deep ocean exchange and anthropogenic CO_2 uptake, *J. Geophys. Res.*, *117*, C10005, doi:10.1029/2012JC008074.

Griffies, S. M., A. Gnanadesikan, R. C. Pacanowski, V. D. Larichev, J. K. Dukowicz, and R. D. Smith (1998), Isoneutral diffusion in a z-coordinate ocean model, *J. Phys. Oceanogr.*, *28*, 805–830.

Gruber, N., J. L. Sarmiento, and T. F. Stocker (1996), An improved method for detecting anthropogenic CO_2 in the oceans, *Global Biogeochem. Cycles*, *10*, 809–837.

Gruber, N., et al. (2009), Oceanic sources, sinks, and transport of atmospheric CO_2, *Global Biogeochem. Cycles*, *23*, GB1005, doi:10.1029/2008GB003349.

Haine, T. W. N., and S. L. Gray (2001), Quantifying mesoscale variability in ocean transient tracer fields, *J. Geophys. Res.*, *106*(C7), 13,861–13,878.

Hegerl, G. C., F. W. Zwiers, P. Braconnot, N. Gillett, Y. Luo, J. M. Orsini, N. Nicholls, J. Penner, and P. Stott (2007), Understanding and attributing climate change, in *Climate Change 2007: The Physical Science Basis. Contribution of Working Group I to the Fourth Assessment Report of the Intergovernmental Panel on Climate Change*, edited by S. Solomon et al., Cambridge Univ. Press, Cambridge U. K., and New York.

Hofmann, M., and H.-J. Shellnhuber (2009), Oceanic acidification affects marine carbon pump and triggers extended marine oxygen holes, *Proc. Nat. Acad. Sci.*, *106*(9), 3017–3022.

Holzer, M., and F. Primeau (2013), Global teleconnections in the oceanic phosphorus cycle: Patterns, paths, and timescales, *J. Geophys. Res. Oceans*, *118*, 1775–1796, doi:10.1002/jgrc.20072.

Holzer, M., F. Primeau, W. Smethie, and S. Khatiwala (2010), Where and how long ago was water in the Western North Atlantic ventilated: Maximim-entropy inversions of bottle data from WOCE line A20, *J. Geophys. Res.*, *115*, C07005, doi:10.1029/2009JC005750.

Houghton, R. A. (2003), Revised estimates of the annual net flux of carbon to the atmosphere from changes in land use and land management, *Tellus*, *55B*, 378–390.

Houghton, R. A., J. I. House, J. Pongratz, G. R. van der Werf, R. S. DeFries, M. C. Hansen, C. L. Quere, and N. Ramankutty (2012), Carbon emissions from land-use and land-cover change, *Biogeosciences*, *9*, 5125–5142, doi:10.5194/bg-9-5125-2012.

Jacobson, A., S. Fletcher, N. Gruber, J. Sarmiento, and M. Gloor (2007), A joint atmosphere-ocean inversion for surface fluxes of carbon dioxide: 1. Methods and global-scale fluxes, *Global Biogeochem. Cycles*, *21*, GB1019, doi:10.1029/2005GB002556.

Key, R. M., et al. (2004), A global ocean carbon climatology: Results from GLODAP, *Global Biogeochem. Cycles*, *18*, GB4031, doi:10.1029/2004GB002247.

Khatiwala, S., F. Primeau, and T. Hall (2009), Reconstruction of the history of anthropogenic CO_2 concentration in the ocean, *Nature*, *462*, 346–350.

Khatiwala, S., et al. (2013), Global ocean storage of anthropogenic carbon, *Biogeosciences*, *10*, 2169–2191.

Large, W., J. McWilliams, and S. Doney (1994), Oceanic vertical mixing: A review and a model with a nonlocal boundary layer parameterization, *Rev. Geophys.*, *32*, 363–403.

Le Quéré, C., et al. (2007), Saturation of the southern ocean CO_2 sink due to recent climate change, *Science*, *316*, 1735–1738.

Locarnini, R. A., A. V. Mishonov, J. I. Antonov, T. P. Boyer, H. E. Garcia, O. K. Baranova, M. M. Zweng, and D. R. Johnson (2010), World Ocean Atlas 2009, Volume 1: Temperature, in *NOAA Atlas NESDIS 68*, edited by S. Levitus, U. S. Government Printing Office, Washington, D. C.

Lovenduski, N. S., N. Gruber, and S. C. Doney (2008), Towards a mechanistic understanding of the decadal trends in the Southern Ocean carbon sink, *Global Biogeochem. Cycles*, *22*, GB3016, doi:10.1029/2007GB003139.

Matsumoto, K., and N. Gruber (2005), How accurate is the estimation of anthropogenic carbon in the ocean? An evaluation of the ΔC^* method, *Global Biogeochem. Cycles*, *19*, GB3014, doi:10.1029/2004GB002397.

Mikaloff-Fletcher, S. E., et al. (2006), Inverse estimates of anthropogenic CO_2 uptake, transport, and storage by the ocean, *Global Biogeochem. Cycles*, *20*, GB2002, doi:10.1029/2005GB002530.

Najjar, R., and J. Orr (1998), Design of OCMIP-2 simulations of chlorofluorocarbons, the solubility pump and common biogeochemistry, online document. [Available at http://www.cgd.ucar.edu/oce/OCMIP/design.pdf.]

Oeschger, H., U. Siegenthaler, and A. Gugelmann (1975), A box diffusion model to study the carbon dioxide exchange in nature, *Tellus*, *27*, 168–192.

Pan, Y., et al. (2011), A large and persistent carbon sink in the world's forests, *Science*, *333*, 988–993, doi:10.1126/science.1201609.

Primeau, F., M. Holzer, and T. DeVries (2013), Southern Ocean nutrient trapping and the efficiency of the biological pump, *J. Geophys. Res. Oceans*, *118*, 2547–2564, doi:10.1002/jgrc.20181.

Redi, M. H. (1982), Oceanic isopycnal mixing by coordinate rotation, *J. Phys. Oceanogr.*, *12*, 1154–1158.

Regnier, P., et al. (2013), Anthropogenic perturbation of the carbon fluxes from land to ocean, *Nat. Geosci.*, *6*, 597–607.

Riebesell, U., et al. (2007), Enhanced biological carbon consumption in a high CO_2 ocean, *Nature*, *450*, 545–548.

Sabine, C., and T. Tanhua (2010), Estimation of anthropogenic CO_2 inventories in the ocean, *Annu. Rev. Mar. Sci.*, 2, 175–198.

Sabine, C. L., et al. (2004), The ocean sink for anthropogenic CO_2, *Science*, 305, 367–371.

Sarmiento, J. L., J. C. Orr, and U. Siegenthaler (1992), A perturbation simulation of CO_2 uptake in an ocean general circulation model, *J. Geophys. Res.*, 97, 3621–3645.

Sarmiento, J. L., M. Gloor, N. Gruber, C. Beaulieu, A. R. Jacobson, S. E. M. Fletcher, S. Pacala, and K. Rodgers (2010), Trends and regional distributions of land and ocean carbon sinks, *Biogeosciences*, 7, 2351–2367, doi:10.5194/bg-7-2351-2010.

Schlitzer, R. (2007), Assimilation of radiocarbon and chlorofluorocarbon data to constrain deep and bottom water transports in the world ocean, *J. Phys. Oceanogr.*, 37, 259–276.

Steinkamp, K., and N. Gruber (2013), A joint atmosphere-ocean inversion for the estimation of seasonal carbon sources and sinks, *Global Biogeochem. Cycles*, 27, 732–745, doi:10.1002/gbc.20064.

Sweeney, C., E. Gloor, R. A. Jacobson, R. M. Key, G. McKinley, J. L. Sarmiento, and R. Wanninkhof (2006), Constraining global air-sea gas exchange for CO_2 with recent bomb ^{14}C measurements, *Global Biogeochem. Cycles*, 21, GB2015, doi:10.1029/2006GB002784.

Wang, S., J. K. Moore, F. W. Primeau, and S. Khatiwala (2012), Simulation of anthropogenic CO_2 uptake in the CCSM3.1 ocean circulation-biogeochemical model: Comparison with data-based estimates, *Biogeosciences*, 9, 1321–1336.

Wanninkhof, R. (1992), Relationship between wind speed and gas exchange over the ocean, *J. Geophys. Res.*, 97, 7373–7382.

Wanninkhof, R., S. C. Doney, J. L. Bullister, N. M. Levine, M. Warner, and N. Gruber (2010), Detecting anthropogenic CO_2 changes in the interior Atlantic Ocean between 1989 and 2005, *J. Geophys. Res.*, 115, C11028, doi:10.1029/2010JC006251.

Wanninkhof, R., et al. (2013), Global ocean carbon uptake: Magnitude, variability and trends, *Biogeosciences*, 10, 1983–2000, doi:10.5194/bg-10-1983-2013.

Waugh, D. W., T. M. Hall, B. I. McNeil, R. Key, and R. J. Matear (2006), Anthropogenic CO_2 in the oceans estimated using transit time distributions, *Tellus*, 58B, 376–389.

Waugh, D. W., F. Primeau, T. DeVries, and M. Holzer (2013), Recent changes in the ventilation of the southern oceans, *Science*, 339, 568–570.

Weber, T., and C. Deutsch (2012), Plankton diversity and ocean circulation regulate the ocean nitrogen reservoir, *Nature*, 489, 419–422.